Originals

Experiments in Fluids 23 (1997) 449–462 © Springer-Verlag 1997

Low cost, high resolution DPIV for measurement of turbulent fluid flow

A. M. Fincham, G. R. Spedding

Abstract An optimized cross-correlation based Imaging Velocimetry system is described and its performance is evaluated in numerical and physical experiments. Given a discrete image array pair, the flow seeding and image processing parameters are optimized to maximize displacement accuracy, regardless of the computational cost; collectively these techniques are known as Correlation Imaging Velocimetry (CIV). Order of magnitude improvements over standard DPIV methods can readily be obtained, allowing high resolution measurements to be made with low cost standard resolution cameras. Fundamental limits on the measurable range of length, velocity and vorticity scales are identified, and related to those encountered in homogeneous, 3D turbulence. The current restrictions apply to all imaging velocimetry measurements; some paths for future research that are likely to be profitable are identified, together with some that are not. Extensive use of CIV in this and other laboratories has allowed direct verification of these optimization principals.

1 Introduction

DPIV (Digital Particle Imaging Velocimetry) methods, pioneered by Utami et al. (1984, 1987, 1990, 1991) and Willert and Gharib (1991) have found widespread acceptance and have been applied to a variety of fluid mechanics problems (e.g. Grant 1994). Compared with alternative, laser-based, analog interrogation systems, DPIV methods, relying as they do on non-specialized digital electronics, are both economical and efficient. They are also well-positioned to profit from predictable (commercially driven) advances in technology.

Received: *26 January 1996/Accepted*: *2 April 1997*

A. M. Fincham[1], G. R. Spedding
Department of Aerospace Engineering,
University of Southern California,
Los Angeles, CA 90089-1191, USA

[1] *Present address*: Laboratoire des Ecoulements Geophysiques et Industriels, Coriolis, B. P. 53 X, F-38041 Grenoble Cedex 9, France

Correspondence to: A. M. Fincham

We would like to thank Prof. Ron Blackwelder for initiating this research, and for providing continued support over the years. Funding from the Office of Naval Research, through the Fluid Mechanics program administered by Dr. L. P. Purtel, has made this work possible.

Although the limitations and accuracy of various Imaging Velocimetry (IV) methods have been discussed in certain instances (most notably by Adrian 1988, 1991; Prasad et al. 1992; Westerweel 1993; Cowen and Monismith 1996), a comprehensive and general treatment is lacking. Limits on accuracy are often constrained by the flow parameters themselves, indicating the need for a specific IV error analysis framework.

If DPIV methods are to be successfully applied to turbulence measurement problems, characterized by 3D motion with broad ranges of velocity and length scales, then close attention must be paid to achieving the best possible accuracy, given a certain sampling resolution. In essence, the question is addressed; given a flow phenomenon to be measured, and some specific hardware configuration, what is the maximum amount of useful information that can be extracted by image correlation analysis?

There are three objectives in the paper:

(1) To present and specify a set of algorithms and optimization techniques, that together, can result in order of magnitude improvements in spatial resolution and accuracy over standard methods. The techniques are collectively known as Correlation Image Velocimetry (CIV).
(2) To identify both the causes and consequences of the dominant errors in practical fluid mechanics applications. The analysis is based on CIV, but the major points are quite general, applicable to many IV methods.
(3) To outline a quantitative analysis on the feasibility of measuring fully turbulent fluid flows with IV methods: what Reynolds numbers can be reached, and at what cost?

2 Analysis of errors

2.1 Experiments and simulations

A systematic approach was taken to the development of the CIV system. Individual parameters relating to particles, lighting, algorithms, and fluid vorticity, were isolated. Extensive optimization allowed their effects on the accuracy of the technique to be determined.

2.1.1 Simulations

Randomly distributed numerical particles with Gaussian profiles were projected onto a virtual pixel array (integrating

the intensity distribution over the area of each pixel), the centroids of the particles were translated according to known flow solutions, and the light integration process was repeated. The resulting image pairs were interrogated, and the measured velocity field was compared with the actual flow solution to yield the error as a function of space.

The displacement error was determined as a function of the particle image size, shape, brightness and seeding density. Out-of-plane velocity components were simulated, and the effects of varying the correlation window size, the form of the correlation function, and the correlation peak fitting technique, could then be related to both the image and flow parameters.

The Gaussian particle profile has an intensity distribution, $I(r) = e^{-(r/2\sigma)^2}$, where r is the distance from the center. 2σ had values corresponding to particles diameters d, of 2, 2.83, 4.9, 6.93, 8.49 and 11.3 pixels, where d is measured at the e^{-2} intensity level. The number of particles is non-dimensionalized by the number of pixels in the array to give the number density N in particles per pixel (ppp). N was varied from 0.022 to 0.333 ppp (the conventional measure of *image density* is related to the ppp measure through multiplication by the number of pixels in the interrogation box).

As fluid dynamicists are seldom interested in measuring irrotational flows, the analysis is focused on flows with shear. Solid body rotation used for the experimental tests can be decomposed into two orthogonal simple shear flows. Consequently, simple uniform shearing flows were chosen for most of the simulations. The strength of the shearing is described by the displacement gradient S, which indicates the in-plane deformation that occurs between images S is related to the vorticity by the time interval between images Δt. The vorticity is a constant for the entire field and is given by,

$$\omega = \frac{\partial u}{\partial y} = \frac{\Delta x}{\Delta y \Delta t} = \frac{S}{\Delta t} \tag{1}$$

where the $\frac{1}{2}$ is dropped for the 1D shear case. S was varied from 0.0067 (0.67%) to 0.213 (21%).

2.1.2 Experiments

In order to ensure that the progress of the simulations was constrained to realistic situations, they were paralleled by a series of careful experiments involving both real particles in water, and real particles glued in place on a small turntable. Promising results from the simulations could thus be verified in the laboratory. In practice, many of the parameters in a real CIV experiment, such as lighting, physical particle properties, image acquisition electronics, and general hardware tinkering, as well as the interactions of these with the flow itself, are not easily simulated. The simulated images could be tuned to match the experiments by ensuring that there was both a qualitative and quantitative statistical similarity between the image properties.

The wet experiments were performed in a precisely built 15 cm diameter by 20 cm tall rotating plexiglass cylinder. The speed of rotation was controlled by a stepper motor, and the lighting was provided by a 5 W argon ion laser. The camera (Pulnix TM 745 interline transfer CCD) was mounted under the tank, parallel to its rotation axis. Typically the tank was completely filled with distilled water, the particles under test were added, all air was removed, and the tank was then spun up to a solid body rotation state. The light sheet pulse was created either by a pair of cylindrical lenses and a mechanical chopper, or by using a computer-controlled, oscillating mirror to provide an effectively instantaneous pulse containing several high frequency scans. Static particle tests similar to Prasad et al. (1992) were conducted by gluing white particles onto a black turntable, and acquiring an image before and after rotation through a known angle. Images were captured directly into image memory on an ITI PC-Vision$^+$ frame grabber board. As the exact angular velocity was prescribed beforehand, errors could be evaluated in a similar way to the simulations, once the center of rotation was determined.

2.2 Errors

Provided the particles adequately follow the flow, and are effectively exposed instantaneously (the time of exposure is short relative to the frame interval Δt, and so there is no blurring due to motion), and that there is no optical distortion or contamination of the scattered light before it reaches the pixel array, then errors in the measurement of the particle displacements will depend solely on the accuracy with which the particle image positions can be determined on the image sensor itself. Consequently the uncertainties associated with particle displacements are functions of the pixel sizes and it is appropriate to express CIV errors in pixels units for all spatial measurements. If we make the further assumption of a perfect pixel array, i.e. there are no gaps between pixels, each pixel has equal gain, and the noise in the DAC (and ADC) is negligible (this requires good synchronization between the camera pixel clock and the ADC), then the problem of determining particle displacements is purely an image processing one, that is well modeled by the above described simulations.

2.2.1 Particle images

CIV is a general technique that does not rely on the use of particle images, and in principal, any passive tracer that provides image texture and follows the flow may be used. The use of scalar gradients as flow tracers is a complex topic by itself, and although CIV has been successfully applied to Laser Induced Fluorescence (LIF) images, even in simple 2D flow fields the associated error analysis is non-trivial and will not be discussed further here. Since particles can provide excellent image contrast and texture in practice, and since their properties can be specified exactly in simulations, the following analysis is centered around particle images. Image exposure is a critical phase of the data acquisition process; being the front end of the process there is little opportunity to correct for mistakes made at this stage. Depending on the light scattering properties of particles, and the optics in use, particle images can be significantly larger than the physical particles that they represent. Experimental details of physical particles properties and lighting systems can be complex, and will not be discussed here, (cf. Adrian 1991). Instead, attention will be focused on the properties of the particle *images*.

To maximize the information content of the images, the pixel intensities should cover the allowable range (0–255 for 8 bit digitization). This is typically done by examining the image histograms and making the appropriate adjustments to the apparatus, or frame-grabber gain and offset. The contrast should be maximized to provide particle images that are distinctively brighter than the background, without saturating the particle profiles. Reflections and glow from dirty water can seriously reduce the contrast, and it is important to ensure that light from anything other than the particles does not reach the image sensor. Proper normalization of the correlation function can apply equal weighting to *all* texture in the image, and the dark background can be just as important as the bright particles in producing strong correlation peaks. Therefore, any light from stationary objects, such as the background, or streaking of the laser sheet, will correlate with itself, resulting in a tendency towards zero displacement correlation peaks. Having a distribution of particle sizes can improve performance, as each local image pattern box will have a better chance of being unique.

Image pre-processing can only serve to destroy or rearrange information as new information clearly cannot be added after the experiment. Provided the above-mentioned precautions are taken during the image exposure process, then there should be no reason to alter the original images prior to the image correlation analysis. Clearly, whenever there is systematic, predictable contamination on the images, such as the presence of towing wires or boundaries, it can be removed beforehand.

2.2.2 Form of errors

All DPIV methods result in a characteristic variation of error with displacement. The error in the displacement, $\Delta D = D_{\text{meas}} - D_a$, is shown as a function of the actual displacement, D_a, in Fig. 1. The abscissa indicates the phase of the error, whose signal is periodic in nature, with a random component superposed on the phase averaged mean, Similar results are obtained for both the experiments and the simulations. This is due to "peak-locking", an effect to be discussed in detail in Sect. 3.1.3. It will prove useful to decompose the error into a periodic mean-bias part, E_{mb}, and the scatter around this local mean, E_{rms}. Each vector is binned according to the fractional part of its actual displacement, so for *nbins* covering the range [0, 1] the bin number is given by, $j = \text{nint}(nbins \times (D_a - \text{int}(D_a))$. The amplitude of the mean bias component of the error is determined from the average error of the n_j vectors in each bin,

$$E_{\text{mb}}(j) = \frac{1}{n_j} \sum_{i=1}^{n_j} \Delta D(i,j) \tag{2}$$

The rms of the remaining fluctuations about this mean is

$$E_{\text{rms}}(j) = \left[\frac{1}{n_j} \sum_{i=1}^{n_j} (\Delta D(i,j) - E_{\text{mb}}(j))^2 \right]^{1/2} \tag{3}$$

The true rms error of each bin, is evaluated as,

$$E_{\text{true}}(j) = \left[\frac{1}{n_j} \sum_{i=1}^{n_j} \Delta D(i,j)^2 \right]^{1/2} \tag{4}$$

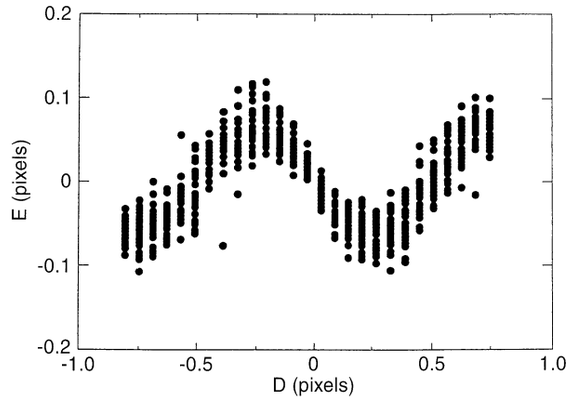

Fig. 1. Error in pixels vs. displacement for simple shear flow, $N = 0.55$ ppp, $d = 3$ pixels, and $S = 0.007$

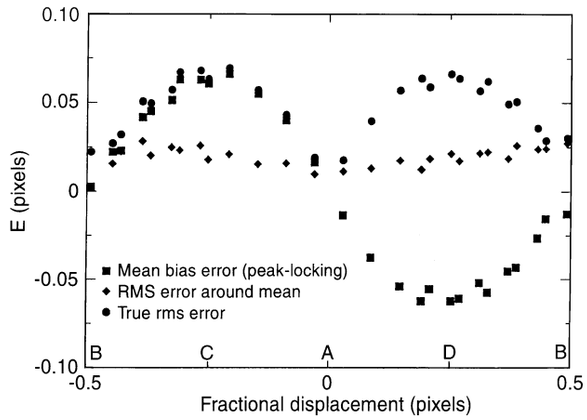

Fig. 2. The phase-averaged error of non-integer pixel displacements is not random, but is a regular (doubly periodic) function of real displacement. There is also significant fluctuation about the mean error curve. These results occurred in both simulations and experiment

E_{true}, E_{mb}, and E_{rms} are shown in Fig. 2 as a function of the fractional displacement. To simplify the following analysis, the error components are averaged over their phase as follows.

$$E_{\text{mb}} = \left[\frac{1}{nbins} \sum_{j=1}^{nbins} E_{\text{mb}}(j)^2 \right]^{1/2}$$

$$E_{\text{rms}} = \frac{1}{nbins} \sum_{j=1}^{nbins} E_{\text{rms}}(j) \tag{5}$$

$$E_{\text{true}} = \frac{1}{nbins} \sum_{j=1}^{nbins} E_{\text{true}}(j)$$

In this way the variances of the error components provide single measures of their importance in each test. For the example in Fig. 1, the value of E_{mb}, E_{rms} and E_{true} are 0.046, 0.020 and 0.051 pixels respectively. Note that $E_{\text{rms}}^2 + E_{\text{mb}}^2 \cong E_{\text{true}}^2$ even though the amplitude of E_{rms} depends on the phase, and the relative importance of the contributions of

E_{mb} and E_{rms} to E_{true} is preserved. Decomposition of the error in this way requires large samples for reasonable statistical convergence. Samples of over 200 000 vectors were used for most of the following results, rendering statistical undersampling errors insignificant.

3
The CIV method

CIV, first introduced in Fincham et al. (1991), has been developed over the course of several years with the constant underlying design objective, that the best possible accuracy and spatial resolution are to be achieved regardless of the computational cost, ensuring that optimum use is made of limited resolution data. The continued and fixed emphasis on accuracy and resolution has yielded surprisingly accurate reconstructions from only modest CCD arrays, rivaling that of much more expensive equipment. Moreover, at any foreseeable resolution, there will always be interest in limiting discretisation errors, so these considerations will not be made obsolete by advances in technology.

3.1
Algorithms for improved accuracy

CIV is based on generalized texture mapping functions, and not on the identification or presence of individual particles, but rather on the fact that under suitable conditions, groups of particles or regions of image texture, will retain similar appearances under small translations and deformations. The particles can then be tracked as a group using a 2D correlation function to perform pattern matching as a function of the displacement D. The actual displacement is determined from the location of the maximum value of the correlation function in the image plane, and is always done to sub-pixel accuracy, with a local curve fit of the correlation data. If the correlations are performed correctly, the maximum value represents the most likely displacement of the image in each interrogation window during the time interval Δt. The correlation algorithm performs a local computation, and each velocity vector is computed independently; there is no accumulation of errors across the field. No assumptions about conservation of mass or particles are required; it is purely a pattern matching algorithm and is not constrained by boundaries or complex flow geometry.

The performance analysis is based upon the cross-correlation method, but many of the arguments apply equally to auto-correlation technique. The auto-correlation suffers from both a decreased signal-to-noise ratio, and a reduced dynamic range. The cross-correlation should therefore be used whenever both the fluid mechanics and economics permit. With the advent of frame buffer-equipped, progressive scanning, interline and full frame transfer CCD cameras, capable of capturing two images only a few micro seconds apart, auto-correlation methods need only be used in very high pixel velocity flow situations, or when high resolution photographic image recording is being employed.

3.1.1
De-coupled box size/search radius

One of the most important features differentiating CIV from standard DPIV is the de-coupling of the sampling box from its fixed location in image #1 to any arbitrary location in image #2, Fig. 3. This general block matching approach is not new and extensive examples and discussions of its use can be found in both the image processing and fluid mechanics literature (Jain and Jain 1981; Gilge 1990; Fuh and Maragos 1991; Utami and Blackwelder 1991; and Huang et al. 1993). This process completely eliminates the velocity bias error[1] first described by Adrian (1986, 1992), and extensively analyzed and corrected for by Westerweel (1993). It greatly improves the signal to noise ratio in the presence of large displacements, significantly extending the dynamic range of the velocity measurement. More importantly, it allows the use of relatively small sampling boxes, which significantly increases the available spatial resolution and reduces the errors encountered when measuring vortical flows. The following describes this process in more detail.

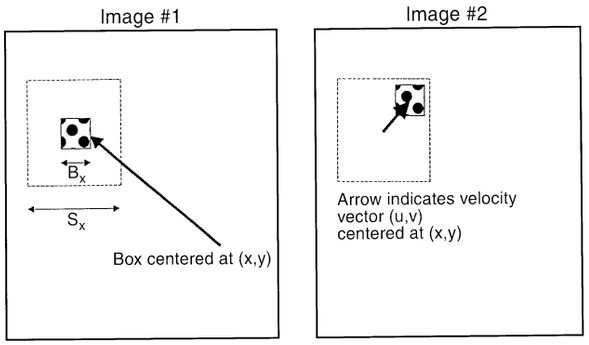

Fig. 3. The decoupled pattern correlation box and search radius

Two images are captured a time interval Δt apart. Image #1 is subdivided into small pattern boxes of size B_x by B_y pixels. During the time interval Δt, the motion of the fluid containing the particles imaged in each of the pattern boxes is restricted by the maximum possible flow velocity. If Δt is short compared to the out-of-plane velocity convective time, δ/w, where w is the out-of-plane velocity component and δ is the light sheet thickness, then most of the particle images contained in a pattern box of image #1 centered at image coordinates (x, y), will appear in image #2 within a search box of size $S_x = 2u_{max}\Delta t + B_x$, by $S_y = 2v_{max}\Delta t + B_y$ pixels, where $\{u_{max}, v_{max}\}$ are the estimated maximum in-plane flow velocities in pixels per second. Further, considering the effects of velocity gradients in x, if both Δt and B_x are small enough to restrict the maximum in-box deformation,

$$\Delta B = \left|\frac{\partial \vec{u}}{\partial x}\right|_{max} B_x \Delta t$$

where B_x can be replaced by δ for the out of plane gradients, to some fraction of the particle image diameter d, then the group of particle images within each box will retain a similar geometric relationship to one another, and effectively undergo a simple translation.

[1]This error results in standard DPIV codes where the position of the pattern box is fixed in both images. Particles with larger velocities can leave the fixed pattern box resulting is a bias towards smaller velocities when there is significant variation of the velocity within the box.

The cross-correlation function $c(i,j)$, between a box in image #1 and the same sized shifted box in image #2 is computed for i in the range;

$$\left\{-\frac{S_x-B_x}{2},\ +\frac{S_x-B_x}{2}\right\}$$

and, j in the range;

$$\left\{-\frac{S_y-B_y}{2},+\frac{S_y-B_y}{2}\right\}$$

where (i,j) represents the relative shift, and covers all possible locations of the sample box within the search box in image #2. Provided there is no larger random correlation, the indices of the maximum value of the correlation, $c_{\max}(i_{c_{\max}}, j_{c_{\max}})$ will correspond to the mean integer shifted position of the particles within the box during the time interval Δt. $c(i,j)$ is computed for each of the pattern boxes in image #1.

3.1.2 Normalization by variance

Most DPIV systems use FFT's to perform correlations between matching regions in each image pair. However, as errors can be quite sensitive to the choice of pattern box size and shape, systems based on FFT algorithms, that, for purposes of rapid computation, impose constraints such as $m=n=$ even, etc., cannot easily be optimized or adapt correctly to changing flow structure. Explicitly performing the correlations in real space gives complete flexibility in the choice of pattern-box sizes and shapes. Extensive tests involving different forms of the correlation function and its normalization were conducted. A variance normalization proved to be the most accurate and robust to the loss of particles between images, results in agreement with those of Burt et al. (1982).

The variance normalized correlation or covariance $c(i,j)$ is defined as

$$c(i,j)=\frac{\sum_{k=1}^{B_x}\sum_{l=1}^{B_y}(I_a(k,l)-\bar{I}_a)\,(I_b(k+i,l+j)-\bar{I}_b)}{[\sum_{k=1}^{B_x}\sum_{l=1}^{B_y}(I_a(k,l)-\bar{I}_a)^2\sum_{k=1}^{B_x}\sum_{l=1}^{B_y}(I_b(k+i,l+j)-\bar{I}_b)^2]^{1/2}} \quad (6)$$

where $I_a(1,1)$, $I_b(1,1)$, represent the pixel intensities at the corner, of a pattern box of size B_x by B_y, centered at image coordinates (x,y), in images #1 and #2 respectively. The quantities $\bar{I}_a$ and $\bar{I}_b$ represent the mean intensity in the sample box of image #1 and the current test box in image #2;

$$\bar{I}_a=\frac{1}{B_xB_y}\sum_{k=1}^{B_x}\sum_{l=1}^{B_y}I_a(k,l)$$

and;

$$\bar{I}_b=\frac{1}{B_xB_y}\sum_{k=1}^{B_x}\sum_{l=1}^{B_y}I_b(k+i,l+j)$$

This type of normalization can give equal weighting to each pixel in the interrogation window, such that the background is just as important as the particle images. It is a pattern matching algorithm, and it is very important that all image intensity variance, or texture motion be associated with fluid motion.

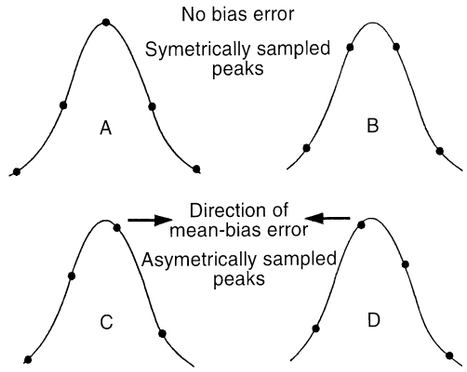

Fig. 4. The peak-locking mechanism causes a bias towards the nearest high data point. The letters a–d are also indicated in Fig. 2

3.1.3 Peak fitting

The search procedure of Sect. 3.1.1 for locating the maximum of $c(i,j)$ gives the nearest integer displacement. This coarse approximation must now be refined to give the best sub-pixel estimates. The accuracy with which the true correlation peak displacement can be estimated *entirely* determines the maximum accuracy and practical utility of *all* IV methods, including CIV.

Recall the general form of the error as a function of displacement, shown in Figs. 1 and 2. The relative error in estimating a continuous function from its discretely-sampled approximation is strongly dependent on the information distribution about it. If the discrete data have reflective symmetry about the true peak location, then the error in peak location is minimized. In all other cases, the non uniform information distribution with respect to the true peak location leads to a bias that pulls the peak estimate towards the closest high data point. The amplitude of this bias error is strongest when the asymmetry is most pronounced, at true pixel shifts of 1/4 or 3/4, as shown in Fig. 4.

We term this phenomenon *peak-locking* and note two points: 1. The peak-locking error can be large compared with the other random components. 2. Since it has a semi-regular shape, it ought to be possible to remove it. Unfortunately, it is not possible to simply subtract the periodic, phase-averaged component of Fig. 2 from all computed correlation shifts, because the amplitude and phase depend on the image quality and local fluid shear. Attention has turned instead to improving the peak-fitting algorithm.

The literature contains many examples of interpolating or peak-fitting functions, (Willert and Gharib 1991; Prasad et al. 1992; Westerweel 1993; Lourenco and Krothapalli 1995; Cowen and Monismith, 1996), but little agreement as to the best one. The contradictor results indicate that although the cause of the peak-locking has been identified by Westerweel, no adequate, general solution is imminent. Amongst common alternatives, we have tested and discarded all center of brightness or centroiding techniques, which are sensitive to arbitrary choices in the cut-off threshold, produce large random errors that depend on the correlation peak characteristics, and show

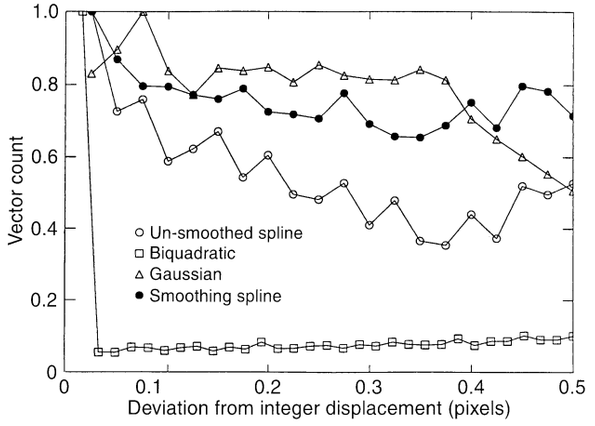

Fig. 5. Distribution of measured fractional displacements for a simple shear flow, using some different peak-fitting functions. The tendency toward integer displacements can be very strong

strong peak-locking for smaller particles (Prasad et al. 1992). Biquadratic, or higher polynomials result in very large peak-locking errors and should not be used. Various spline approximations perform better, but are sensitive to small errors in the data and still suffer from strong peak-locking tendencies. Symmetric or asymmetric Gaussians can perform quite well under favorable conditions, but their dependence on the fit weighting functions can make the results inconsistent, showing inverse peak-locking in some cases. The thin-shell, smoothed spline functions described by Spedding and Rignot (1993) although far from perfect, were chosen for this analysis as they show no disposition towards the Gaussian particle image profiles, and the smoothing parameter, ρ, can be adjusted to effectively randomize the phase of E_{mb}, decreasing the susceptibility to peak-locking errors. A comparison of some different peak-fitting functions is shown in Fig. 5, which shows the distribution of the fractional part of the *measured* displacement for a simple shear flow. A perfect peak fit would give equal probability for all fractional displacements, but a tendency towards integer displacements is observed in all cases. Both the smoothing spline and the Gaussian perform acceptably under the same conditions. Care should be taken in interpreting these results as they say nothing about the true errors associated with the different fits, and large random errors can easily scramble the phase of the bias-error, making peak-locking undetectable. Figure 5 is provided solely to illustrate the peak-locking phenomenon and to demonstrate the use of displacement distribution function analysis for its detection in real data.

The presence of the peak-locking phenomenon is relatively independent of the correlation algorithm used and will appear (in some form) in *any* type of IV technique where sub-pixel determination of the displacement vector is attempted. The effects are especially visible when measurement of vorticity is attempted, showing up as ripples on the vorticity field that can exceed the real vorticity in amplitude. Although the smoothing spline fit compares favorably, there is no *a priori* reason to expect it to be an optimum choice, as the imposed functional form for the correlation distribution has no physical basis. Current research indicates that significantly better assumptions can be made, and will be the subject of a separate paper.

3.2 Basic optimization for simple shearing flows

3.2.1 Optimum particle image size, number density & the effects of shear

As the CIV method relies on image texture and contrast, each particle image size will have associated with it an optimum seeding density N_{opt}. Stronger shear may require higher seeding densities to account for the variation of velocity within the sample box, further complicating the optimization problem.

To simplify the analysis we focus on mono-dispersive particle seedings and investigate $N_{opt}(d)$. Figure 6b shows the decomposed error in pixels vs. the particle number density N, for a moderate deformation, S, of 0.107, and a particle diameter d of 4.9 pixels. The true errors are very large for low particle seeding densities. They reach a minimum but slowly increase as image texture is drowned by the large number of particles. The error is clearly dominated by E_{rms} for all N. For the lower shear of 0.027 with the same particle diameter, Fig. 6a, E_{true} is smaller and shows a minimum around $N=0.05$ ppp. The

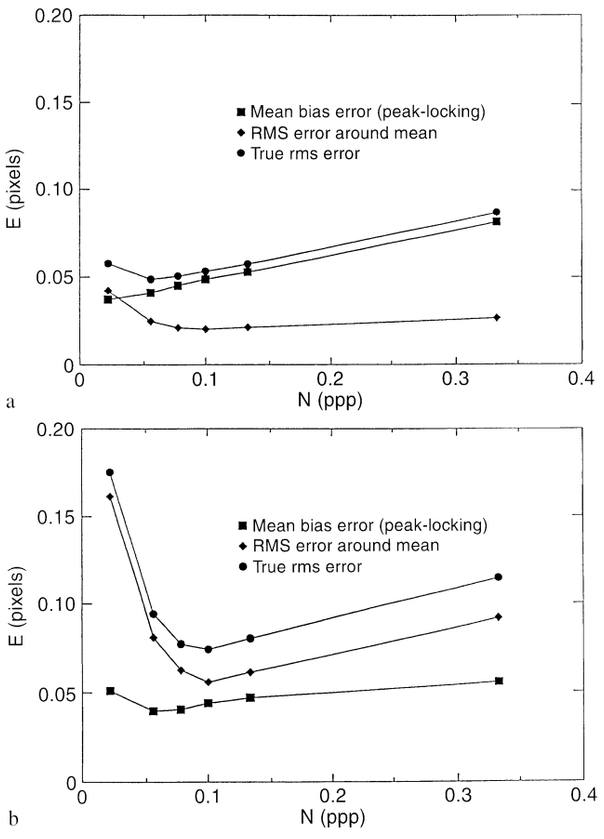

Fig. 6a, b. Error as a function of seeding density. **a** $S=0.027$; **b** $S=0.107$

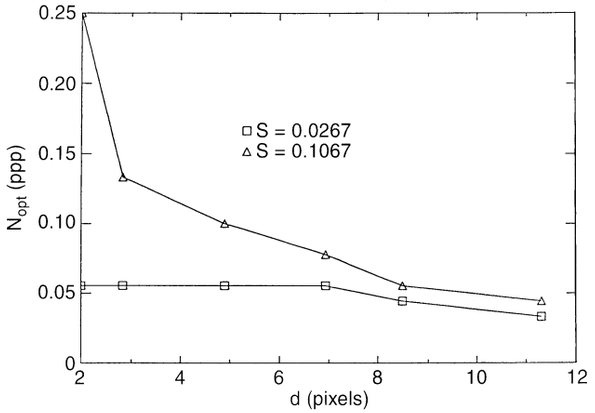

Fig. 7. Optimum seeding density vs. particle diameter, for strong and weak shear

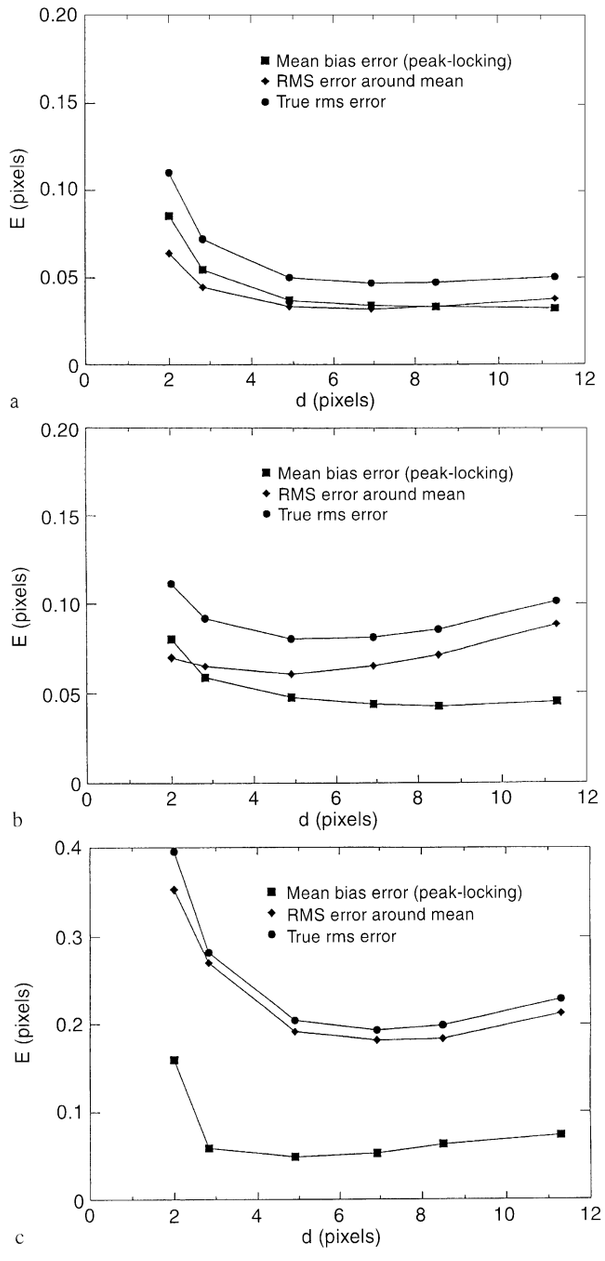

Fig. 8a–c. Error vs. particle diameter using the optimum N values from Fig. 7. **a** $S=0.027$; **b** $S=0.107$; **c** $S=0.213$ (note: change of scale in E)

increase in error with N is now determined by E_{mb}, while E_{rms} shows a sharp decline then remains fairly constant for N greater than 0.1 ppp.

Using the simulation data base, the optimum seeding density was determined for each particle diameter for different shears. Same results are shown in Fig. 7, where it is clear that for weak shearing, the seeding density is not very critical, while for stronger shear, smaller particles require larger number densities. The optimum seeding densities reported here are significantly larger than those reported by other researchers Willert and Gharib (1991) and Westerweel (1993). This reflects the need to maximize the information content of the relatively small pattern boxes, in agreement with results of Utami and Blackwelder (1991). In essence, *any* untextured background can be thought of as wasted signal. It should be noted that in practice, these high seeding densities can be difficult to achieve, issues related to the effective transparency of the fluid and the physical properties of the particles themselves often place the first limits on usable seeding densities.

Using the optimum seeding density, N_{opt}, for each value of d, the independent effect of variation of d and S on the error can be seen in Fig. 8a–c. The lowest error is achieved for $d \cong 6$ pixels, for all $S \in [0.02, 0.22]$, over an order of magnitude variation in S. Nontheless in the high shear case (Fig. 8c) it is evident that the consequences of using too small a particle are quite severe. As the local shear is increased, fluid elements are increasingly deformed over the time interval Δt. If the deformation within the sample box, $\Delta B = SB/2$, becomes of order d, the particle image pattern pairs have a sharply reduced degree of overlap, and the correlation amplitude decreases. For the conditions, of these tests, such a cutoff can be predicted when $d=2$ pixels for $S=0.213$, consistent with the sharp rise in error in Fig. 8c. Once again in Fig. 8, E_{rms} dominates at higher shearing rates. Results based on simple models for E_{mb}, and E_{rms} Prasad et al. (1992) show similar trends but indicate an optimum particle diameter between 2 and 3 pixels. Their results, based on centroidal fitting of a perfect 1D Gaussian require multiplication by a factor $\sqrt{2}$ for comparison as they square the correlation function. They have not accounted for the presence of shear, and assume $E_{mb} \to 0$ for $d > 2.5$. These factors are likely to increase the optimum value of d, moving it reasonably close to the one reported here.

The form of the correlation peak is closely related to the shape and size of the particle images (Westerweel 1993), and as the particle diameter increases so does the correlation peak width. A better resolved correlation peak reduces E_{mb} for

larger d, as seen in Fig. 8 (note: in Fig. 8c the slight increase in E_{mb} for large d is due to leakage from the large amplitude rms component, which cannot be so easily isolated.)

The requirement for increasing d with increasing S creates a dilemma for the experimentalist trying to measure highly vortical flows, for strong vorticity is usually associated with small scales, yet apparently we need large particles to measure them. In practice, large particle *images* can be attained without interfering with the flow, either by using highly reflective particles whose image is diffraction limited, or by defocusing smaller particles (Browand and Plocher 1985).

3.2.2
Effects of box size

Particle size and seeding densities must be determined before the experiment is performed. For a given flow, S depends only on the choice of Δt and can be adjusted either during the experiment, or possibly afterwards if many redundant frames are captured. By contrast, the sample box dimensions B_x and B_y can always be optimized at leisure after the experiment. They can be chosen so as to preserve square fluid elements in cases where the camera pixels are not square, or, in flows with strong anisotropy, rectangular boxes can be chosen to provide spatial resolution in the direction it is needed while maintaining a reasonable total area for each box. Smaller box sizes provide better spatial resolution, but as they contain less information will result in larger random errors. Figure 9a–c shows the effect of changing the box size B, for $S=0.027$, 0.107 and 0.213 respectively. For weak shear, Fig. 9a, there is a gradual decrease in E_{true} with increasing box size, due to the reduction in E_{rms} with the increased information content of the larger boxes. E_{mb} remains unchanged and eventually limits the accuracy.

For $S=0.107$, E_{rms} starts to dominate and there is a reduction of E_{mb} due to the effects of the shear scrambling the phase of the error. E_{true} shows a minimum for $B=18$ pixels. For even stronger shear, $S=0.213$, there is total domination by E_{rms} and the larger boxes perform quite badly as the deformation at the edge of the boxes ΔB, approaches the particle diameter d. Here the increased error associated with the reduced information content of the smaller boxes is still better than allowing significant distortion within the box. In the presence of shear, smaller boxes increase the mean correlation value, a trend that can be used to find the optimum box size for experimental data. Box sizes as small as 5×5 pixels have been used successfully under optimal experimental conditions.

In strongly vortical flows, the deformation of the sample box by the in-plane velocity gradients is one of the limits on sub-pixel location of the correlation peak. By using the strain rates computed from a first pass computation of the velocity field, to deform the sample box in image #2 before correlation on a second pass, better matching can be obtained for strongly deformed regions, as analyzed by Fuh and Maragos (1991) and Huang et al. (1993). This is simply an extension from simple translation of the box, to translation plus deformation. Higher order deformations can also be made, analogous to the series expansion approach of Tokumaru and Dimotakis (1993).

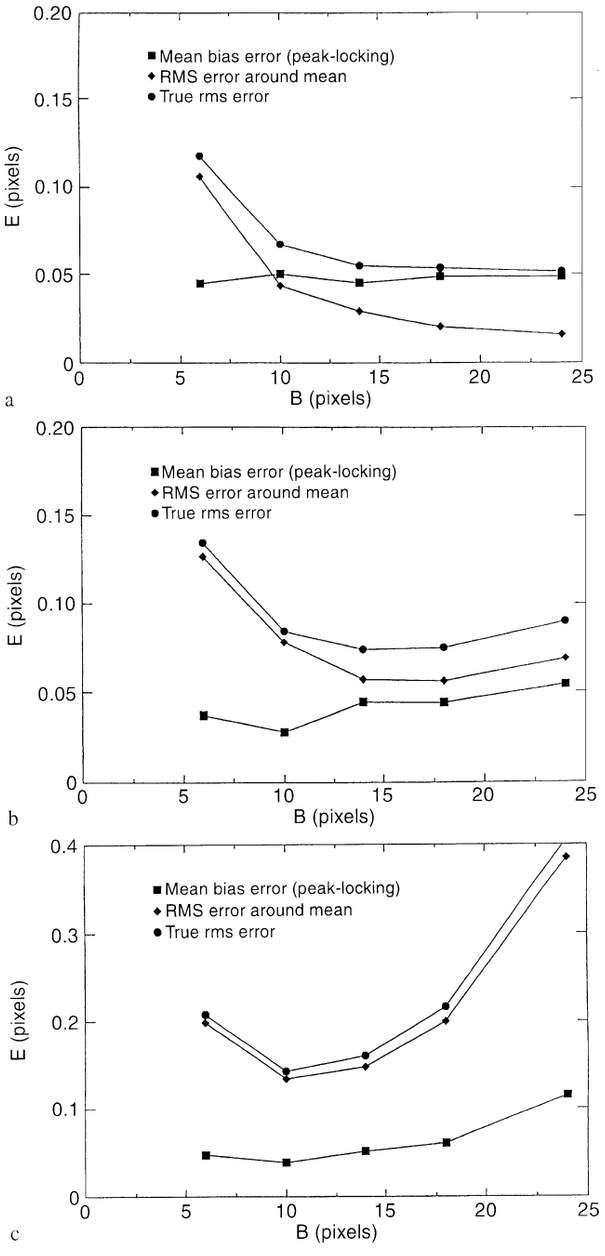

Fig. 9a–c. Error vs. box size. **a** $S=0.027$; **b** $S=0.107$; **c** $S=0.213$ (note: change of scale in E)

3.3
Computation of vorticity

3.3.1
Automated error detection

There is no guarantee that the peak associated with the largest correlation value represents the true displacement of the fluid in the sample box. Especially when the correlations are weak, there is always some chance of a random pattern correlation

giving vectors that are grossly incorrect, or false. These F-vectors will be unrelated to the flow, and should stand out when compared with their neighbors. The probability of random correlations increase for smaller boxes, as they contain less information and are less likely to be unique in the search neighborhood.

A vector correcting routine was developed to post-process the displacement information obtained from the correlation algorithm. The routine compares each vector with its neighbors, computing the relative deviations in both magnitude and direction. The most deviant neighbor is discarded (to allow for adjacent bad vectors), and a single F-factor is computed, and normalized with the deviation statistics from the entire field, which are based on the dot-products of adjacent vectors. Based on a statistically derived threshold, the vector is classified as false. The image correlation for the false vector is recomputed, but the correlation peak corresponding to the F-vector is suppressed in the correlation plane, and the next highest peak is fit, returning a new vector. The process is iterated on the entire field with the statistics being updated after each pass. A lower limit of the correlation value is set for the actual rejection of a perpetually false vector, typically about 30% of the maximum value. Each corrected vector is tagged, and the corrected vector field is output. Still, the procedure is not perfect, and a small number (1–5%) of the F-vectors can slip through the screening process. Westerweel (1994) analyses in detail a number of similar procedures.

The final judgment as to what constitutes a bad vector is actually quite a sophisticated estimate, incorporating fluid mechanical constraints that are not so easy to program. A final stage involving manual inspection of every vector field by experienced fluid dynamists familiar with the flow being studied is necessary.

3.3.2
Re-interpolation, filtering and computation of derivatives

One of the attractions of the CIV-type methods is that the velocity field is apparently evaluated on a regular grid. In fact, displacements computed at each sampling box location, (x, y), are more closely representative of the velocity at the location halfway between (x, y), and the final location of the box, $(x+\Delta x, y+\Delta y)$. Failure to correct for this results in a systematic error in the computation of the spatial derivatives. After the convective correlation, the now irregular grid of velocity data is fit with the same smoothing spline used in the peak fit. The spatial derivatives are computed analytically from the coefficients of the spline functions, thus avoiding errors associated with finite differencing schemes. Provided the ratio of the characteristic length scales in the flow to the original grid spacing (referred to as L/δ in Spedding and Rignot 1993), is large, the rms errors associated with the reinterpolation process will be small.

Pattern boxes can be overlapped to provide a denser coverage of data. Although the overlapping does not increase the true spatial resolution, which is set by B and the light sheet thickness δ by independently evaluating the velocity at scale B for an increased number of nodes, new samples of the original information can be obtained. Each different selection of particles will produce a slightly different correlation peak, allowing random grid scale fluctuation errors associated with E_{rms} to be averaged out by an appropriate spectral filtering technique. The filtering can be done on both the velocity data and its spatial derivatives, or the derivatives can be computed after filtering by re-splining the filtered velocity data. The filter used is typically a 2D fourth order Butterworth low pass filter, where the cut-off wave-number is set to the sample box size.

Spectral filtering of non-periodic data causes contamination by wrap-around through left/right and top/bottom borders. The effect can be significantly reduced with the 'flip-filter' where the data field is replicated by reflection at each border, and once again at the corners, to smoothly fill the eight surrounding squares before applying the filter. Following inversion, only the central rectangle, corresponding to the original grid, is retained. Most contamination is confined to the edges of the expanded data set, and is removed in the un-flipping process. If additional information is available about the velocity field and its spatial gradients, different cut-off-wave-numbers can be used for the different velocity components, or directions.

3.3.3
Reconstruction of Burgers' vortex

In order to examine the actual dynamic range of the vorticity measurement, and to determine the smallest resolvable scales, it is necessary to introduce an independent length scale. Burgers' vortex, is a closed form solution of the Navier–Stokes equations with a Gaussian vorticity distribution defined by $\omega_z = Ce^{-(r^2/r_0^2)}$, where r_0 is the core radius and C represents the strength of the vortex, and was simulated in a way similar to that of the simple shearing flows. The azimuthally-averaged tangential velocity profile, $u_t(|r|)$ of the un-filtered CIV image data for Burgers vortex with $r_0 = 50$ pixels, $\Delta t = 1$ s, and $C = \omega_{\max} = 2S = 0.25$ (for consistency with the 1D simple-shear flow analysis, the 2 in Eqn. (1) is reintroduced) is shown in Fig. 10 along with the Burgers' solution and the true rms deviations. Both the image and processing parameters were chosen based on the optimization arguments of the previous sections, so $B = 15$ pixels, $N = 0.1$ ppp and $d = 6.93$ pixels. By allowing only a 1 pixel overlap in the correlation window, enough statistics were obtained to decompose the error into

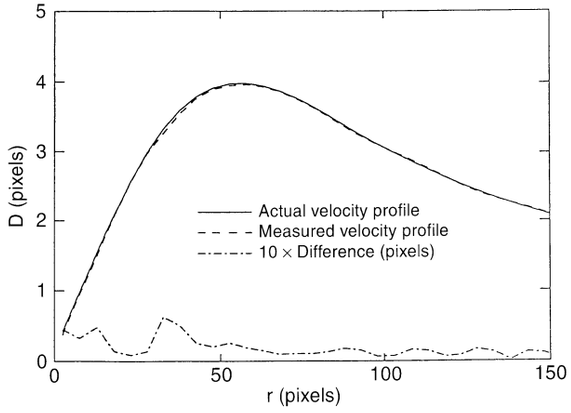

Fig. 10. Reconstructed azimuthally-averaged velocity profile for Burger's vortex, conditions as in Fig. 11

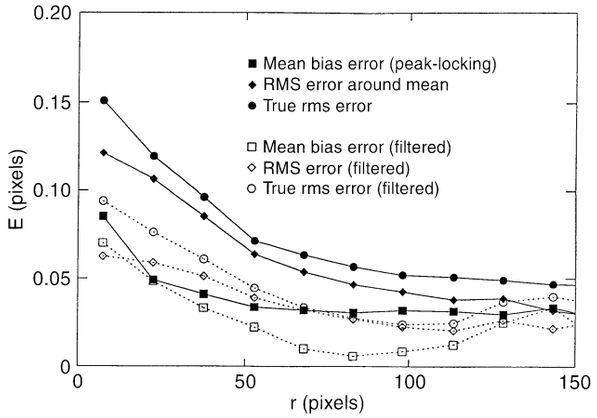

Fig. 11. Decomposed error vs. radius for Burger's vortex, $r_0 = 50$, $C = 0.25$, $B = 15$ pixels and d = 6.93 pixels. Solid symbols are before resplining and filtering the velocity field data. The cut-off wavenumber corresponds to 12.5 pixels

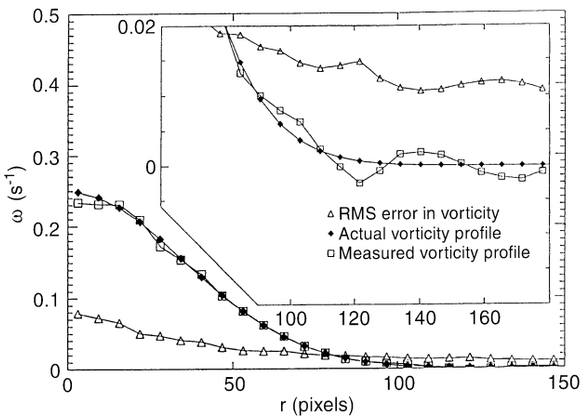

Fig. 12. Vorticity profile from the splined, unfiltered data. Conditions as Fig. 11. (insert shows details of vortex tails)

its mean bias and rms parts as a function of radius. The decomposed displacement errors are shown in Fig. 11. The greatest error occurs in the core where E_{rms} dominates, while E_{mb} shows itself in the weakly sheared tails, consistent with the analysis of Sect. 3.2.1. Also shown are the effects of the spectral flip-filter, where the cut-off wavelength is set to 12.5 pixels. Here we observe a 50% reduction of the errors in the core, due mainly to the quenching of E_{rms}. In the tails, E_{mb} remains relatively unchanged so there is little overall change in E_{true}.

The splined, un-filtered vorticity distribution, $\omega(|r|)$, is shown in Fig. 12 along with the Burgers' solution and the associated rms error in vorticity. There is a clear underestimation of the peak vorticity along with oscillations associated with peak-locking, that are more visible in the detailed view of the vortex tail. The true rms error in vorticity is over 30% in the core and exceeds the measured vorticity at $r = 80$ pixels. The underestimation in the core is associated with the spatial averaging effect of the correlation window where the gradients are large. Application of the spline and spectral filter greatly improves the situation (Fig. 13). Core errors are now below 4%, and the error remains less than the measurement out to

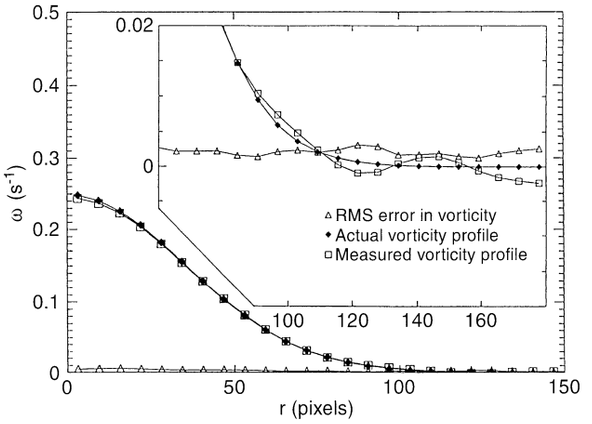

Fig. 13. Vorticity profile for splined and filtered data. Conditions as in Fig. 11

$r = 110$ pixels. Nonetheless, closer inspection shows the amplitude of the peak-locking oscillations in the tails is basically unchanged, and E_{mb} has withstood the filtering process. As the wavelength of these mean-bias error oscillations is unrelated to any of the processing options (it is determined solely by the local vorticity and pix/cm conversion) it is not possible to filter this out in a general manner without seriously distorting the vortex structure. A suitable filter strategy must be spatially-localized, adapting to the local vorticity magnitude, and in principle can be performed on a wavelet basis.

4 Application to turbulence

4.1 Actual errors

4.1.1 Velocity

The experimentalist is usually concerned with the actual percentage rms error in the velocity measurement, and not the pixel errors. The actual error in velocity E_{vel} is given by $E_{\mathrm{vel}} = E_{\mathrm{true}}/|D|$. E_{true} is independent of the displacement $|D|$, depending primarily on the flow parameters S and w, so as $E_{\mathrm{vel}} \sim 1/|D|$, one ought to maximize $|D|$ for any experiment, given certain additional constraints. Displacements greater than the box size result in velocities averaged over distances greater than the grid spacing, and so reduce the effective spatial resolution. As the deformation gradient, S, is related to the vorticity by $S = \omega \Delta t$, increasing Δt will increase S. Figures 8 and 9 show that increasing S will increase E_{true}, significantly increasing the percentage rms errors for all displacements. In flows with large, non uniform accelerations, Δt must be chosen such that $\Delta t\,(\mathrm{d}v/\mathrm{d}t) \ll v$.

A more fundamental limit in D (hence Δt) is caused by out-of-plane velocity components removing particles from the light sheet during Δt. For an out-of-plane velocity, w, the fraction of particles leaving a light sheet of thickness δ in a time Δt is $w\Delta t/\delta$. Out-of-plane motion was simulated by randomly removing and adding particles between image pairs. Figure 14

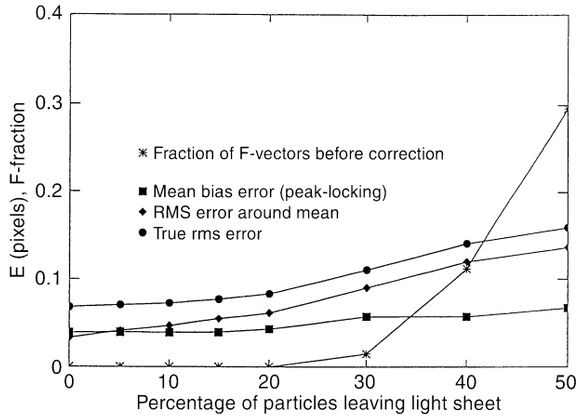

Fig. 14. Effects of out-of-plane motion on the error components. Also shown is the increase in false vectors, all of which were automatically corrected before splining and computation of errors

shows the decomposed errors in D vs. the percentage of particles leaving the light sheet in the interval Δt. As more and more particles are removed from the light sheet and replaced by new ones, an increasing number of vectors are lost to random correlations (also indicated in Fig. 14). The vector correcting algorithm described in Sect. 3.3 proved capable of automatically locating and correcting all the F-vectors in Fig. 14, even when their number densities approached 30%, as is the case for the cross flow corresponding to a 50% loss of particles in Fig. 14. The sharp rise in the number of F-vectors that occurs when 30% of the particles leave the light sheet, is also accompanied by an increase in the error, which is evaluated after vector correction and filtering here. As the robustness of the vector-corrector depends significantly on the flow conditions, a conservative limit of 30% is placed on the maximum tolerable out-of-plane loss of particles.

Applying the 30% criterion to an anisotropic 3D flow, where $|w'| \cong |u'|$ and setting the light sheet thickness $\delta \sim B$ to preserve cubic fluid elements, the maximum sustainable displacement, $D_{max} = u_{max}\,\Delta t$, for $w_{max}\,\Delta t/B = 0.3$, is, $D_{max} = B/3$. For a fixed δ, larger particle seeding densities, or larger pattern box sizes, will allow slightly greater out-of-plane motions. In a fully 3D flow, the maximum sustainable F-vector count typically provides the first constraint on D_{max}, before considerations of in-plane spatial resolution. In quasi-2D flows where $|w| \ll \{|u|, |v|\}$, the only limit on D_{max}, other than the reduced spatial resolution that occurs when $D_{max} > B$, is that eventually the local shear will rearrange the particles beyond recognition by simply translating codes. As the minimum percentage error occurs for the largest displacements it is important to optimize for this. However, due to the rapid rise in the number of F-vectors, the consequence of allowing too large a displacements in single pass translating codes applied to 3D flow is total loss of the measurement.

4.1.2 Vorticity

The percentage error in vorticity, $\Delta\omega'/|\omega| = \Delta S'/|S|$ is independent of $|D|$. Closer examination of the vorticity profiles in Figs. 12 and 13 indicates that there is an increase in $\Delta\omega'$ associated with large $|\omega|$ but also a background level of uncertainty below which $\Delta\omega'$ does not fall. This implies an optimum value of $|\omega|$ where the percentage error in vorticity is a minimum, about $|\omega| = 0.2\,s^{-1}$, or $S = 0.1$ for the unfiltered vorticity profile in Fig. 12. If possible, Δt should be chosen so as to keep S within this range for the vortical structures of interest. A smaller box size reduces $\Delta S'$ in the core, but increases $\Delta S'$ in the tails, implying that B should be a function of S, a process that can be implemented in a multiple pass code. The final judgment as to the choice of Δt, and hence S, depends on the objective of the experiment and flow under study, i.e. is it more important to reconstruct the vortex cores, or to resolve weakly vortical motions in the far field?

The range of S can be extended by acquiring three images at times, t, $t+\Delta t$, and $t+n\Delta t$, choosing Δt and n such that S remains optimal in the core for images 1 & 2, and when S approaches $\Delta S'$ in the tails, images 1 and 3 are used, returning the local S to its optimal value. The errors introduced by the difference in time of evaluation of the vectors in the near and far fields can be avoided by using a 4 image acquisition, $t-n\Delta t$, t, $t+\Delta t$, and $t+(n+1)\Delta t$, allowing the average time of the measurement to be the same for all vectors.

4.2 Measurable range of scales, velocities & vorticities

4.2.1 Velocity

The bandwidth of the velocity measurement is set by the ratio of D_{max} to the smallest tolerable displacement, D_{min}. D_{min} depends on the acceptable error in the low speed regions. $\Delta D'$ can be limited to about 0.05 pixels, and a value of $D_{min} = 0.5$ pixels gives a 10% error. D_{max} depends on the box size, B. In isotropic 3D flows where $\delta \approx B$, this will about $0.3B$, or $D_{max} = 6$ pixels for $B = 18$, providing an effective velocity bandwidth of 12. For a given B, increased velocity bandwidth can be gained at the expense of spatial resolution by increasing the light sheet thickness δ. Larger displacements can be attained, but additional errors associated with shear parallel to the light sheet will be incurred.

4.2.2 Scales

The highest in-plane spatial resolution is ultimately limited by the sample box dimensions, B. Once the first approximation to the velocity field is known, one may reduce the sample box size and recompute the correlations in a small neighborhood around the previously measured mean displacement. This can be thought of as a multi-grid scheme in which two or three passes with decreasing box-sizes are made. The limit depends on the requirement that each box contains some image texture, so high particle seeding densities are required. When B is reduced below its optimum value, determined from Fig. 8, we begin to sacrifice accuracy, or velocity bandwidth, for spatial resolution. Ideally, the box size varies locally with S (as noted in the previous section), allowing an extension of the range of scales, with little compromise in the velocity bandwidth. Burgers's vortex simulations indicate adequate reconstruction of the vorticity field, provided $B \leqslant r_0$, so, conservatively,

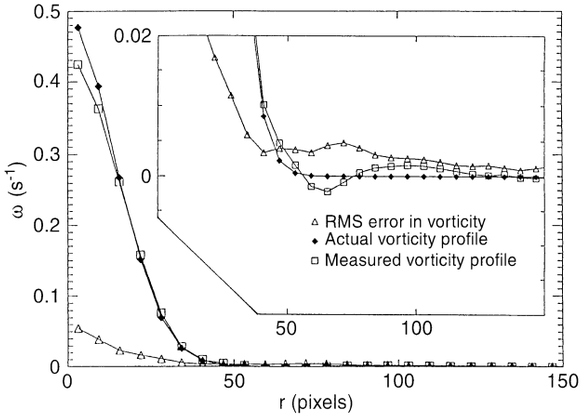

Fig. 15. Reconstructed vorticity profile for Burger's vortex, $C=0.5$, $B=15$, $r_0=20$ pixels

B should be less than half the size of the smallest scale of interest.

The largest resolvable scales are limited by the smallest linear dimension of the sensor array n. The range of measurable scales is then $n/2B$, which is about 15 for a typical 512^2 sensor with $B=18$ pixels, but can be as much as 42, for $B=6$ pixels.

4.2.3 Vorticity

The bandwidth in vorticity measurements is S_{max}/S_{min}, where S_{max} and S_{min} represent the largest and smallest values for which $\Delta S'_{max}/S_{max}$ and $\Delta S'_{min}/S_{min}$ are below some acceptable threshold. The fundamental maximum limits on S are due to the angle of rotation of the fluid element (in this steady flow), and the ability to obtain an adequate correlation peak with a simple translation code. For Burger's vortex, $S=1$ corresponds to a rotation of 1 radian, where the curvature of the particle path lines start to be important in determining the velocity. Limiting S to 0.25 reduces the error to less than 1% and the corresponding uncertainty $\Delta S'_{max}$ in the reconstructed, filtered vorticity field produces an acceptable value for $\Delta S'_{max}/S_{max}$ of 10%, giving a maximum tolerable shear $S_{max}=0.25$ (Fig. 15). The error in measurement of weak vorticity is governed mainly by peak-locking errors, generating background oscillations with amplitudes of $\Delta S'_{min}=0.001$ (Figs. 12, 13, 15), requiring $S_{min}=0.01$ for a 10% error. The useful dynamic range is therefore about 25.

4.3 Can DPIV measure high Re turbulence?

4.3.1 The dynamic range of turbulence

The preceding length, velocity and vorticity range arguments can be related to those encountered in a real turbulent flow, through scaling which we briefly review and develop here. Assume high Reynolds number, isotropic, homogeneous turbulence, with integral quantities U' and L, and turbulent energy spectrum $E(k)$. For a fully developed inertial range, as described by Kolmogorov (1941), the energy spectrum is determined entirely by the energy dissipation $\mathscr{E}$ and has the form

$$E(k)=C_K\mathscr{E}^{2/3}k^{-5/3}, \text{ where } C_K\approx 1.5.$$

If the large scales are assumed to transfer all of their energy in a single eddy turnover time, then the dissipation, $\mathscr{E}$ can be approximated by, $\mathscr{E}\approx U'^3/L$. The velocity u, that is associated with an eddy of scale l, and wavenumber k_l, where $k_l=2\pi/l$ is given by

$$\frac{1}{2}u^2=\int_{k_l+\Delta t}^{k_l-\Delta k}E(k_l)\,\mathrm{d}k \tag{7}$$

For a *simple* eddy $\Delta k\approx k/2$ (see Tennekes and Lumley 1972, p. 258), and,

$$u^2\cong 2E(k_l)k_l=2C_K\frac{U'^2}{L^{2/3}}k_l^{-2/3} \tag{8}$$

The range of scales can then be related to the range of velocities by

$$\left(\frac{u}{U'}\right)^2\cong\frac{2C_K}{(2\pi)^{2/3}}\left(\frac{l}{L}\right)^{2/3}\cong 0.88\left(\frac{l}{L}\right)^{2/3}$$

$$\text{or, } \frac{u}{U'}\cong\left(\frac{l}{L}\right)^{1/3} \tag{9}$$

$$\text{and, } \frac{\omega_l}{\omega_L}\approx\frac{u/l}{U'/L}\cong\left(\frac{L}{l}\right)^{2/3} \tag{10}$$

So three decades of inertial range wave-number will correspond to two decades of vorticity and one decade in velocity.

4.3.2 Fundamental limits

Limits will arise in *any* IV method, if one attempts to preserve cubic fluid elements by requiring, $\delta\leqslant l_d/2\approx B$, where the dissipation scale l_d, represents the smallest scales of interest and δ is the light sheet thickness. The maximum velocity, $U\sim U'$, is associated with a physical displacement, $D_{max}=U\Delta t\leqslant\delta/3$, (from the analysis of Sect. 4.1.1) where the factor of 3 is a hard limit, that at best could be pushed to 2, allowing only a 50% signal recovery (note: for holographic, or other 3D measurement systems, it can be 1). Consequently, $\Delta t_{max}=\delta/3U$. The maximum vorticity in the flow will be associated with scales of size l_d and velocity u_d, so $\omega_{T\,max}=2u_d/l_d$, and the maximum shear, $S_{T\,max}=u_d\Delta t/l_d$. Likewise, the vorticity associated with the integral scale structures corresponds to the minimum shear of interest, $S_{T\,min}=U\Delta t/L$. Substituting for Δt,

$$S_{T\,max}=u_d\delta/3Ul_d, \text{ and } S_{T\,min}=\delta/3L \tag{11}$$

In order to properly resolve the small scales we require, $2B\leqslant l_d$, so, $S_{T\,max}\leqslant u_d\delta/6UB$. Finally for cubic fluid elements, $\delta=B$, and,

$$S_{T\,max}\leqslant u/6U, \text{ and } S_{T\,min}\leqslant l_d/3L \tag{12}$$

indicate the upper and lower limits on the deformations to be encountered in such a flow.

The full range of scales present can be expressed in terms of the Taylor microscale Reynolds number, Re_λ,

$$\frac{L}{\eta} \cong 15^{-3/4}\,\mathrm{Re}_\lambda^{3/2}, \text{ (Hinze 1975)} \qquad (13)$$

where η is the Kolmogorov microscale. Assuming $l_d = 10\eta$ (Monin and Yaglom, 1975), $S_{T\min}$ and $S_{T\max}$ can be expressed as a function of Re_λ using Eq. (9), and are plotted in Fig. 16. Recalling the limits on accurately measurable S developed in Sect. 4.2.3, $S_{\min} = 0.01$, and $S_{\max} = 0.25$, it becomes clear that although we currently have required dynamic range in velocity for $\mathrm{Re}_\lambda = 3000$, the associated shear is well below the experimentally desirable threshold for accurate determination, and the optimum shear value of $S = 0.1$ cannot be achieved. The full entropy field can only be resolved for $\mathrm{Re}_\lambda < 200$, and the limit comes from the mean-bias/peak-locking errors that restrict the accuracy of determining the correlation peak location, and *not* from the deformation of the sample box by shear.

4.3.3 What can be done

The conclusion that high Re, 3D turbulent flows cannot be accurately measured by current IV methods is a little depressing, but leads us to inquire how future research efforts should be concentrated. Given the constraints, the only solution is to reduce the errors associated with measuring small velocity gradients (improve subpixel accuracy), i.e. to lower the $S_{\min}$ line in Fig. 16.

Figure 16 is correct provided one insists on measuring all significant scales of motion (luckily, we need not necessarily resolve the dissipation scales down to η, as required in DNS). By relaxing the constraint that $\delta \leqslant l_d/2$, (i.e. allowing $\delta > B$) it is possible to increase Δt hence, $S_{T\min}$ and $S_{T\max}$, making better use of the available vorticity bandwidth, but the now-rectangular fluid elements will contain errors incurred in averaging their projected velocity components. It is possible however, to relax $\delta \leqslant l_d/2$, and then, *zoom out*, keeping $B \approx \delta > l_d/2$, accepting the effects of averaging smaller scales within the box, and resolving scales from 2δ up. This approach does not come without cost, as the increased Δt will eventually drive $S_{T\max}$ above $S_{\max}$, physically corresponding to the highly vortical motions of size l_d scrambling the particle images beyond recognition.

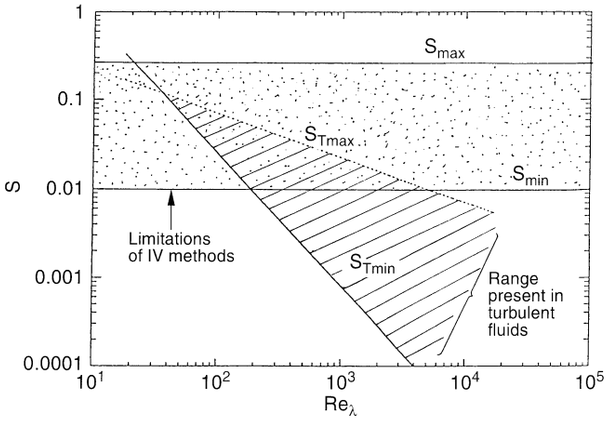

Fig. 16. The fundamental limits of IV-methods can be expressed as constant values of maximum and minimum measurable shear, ($S_{\max}$, $S_{\min}$) as explained in the text. With increasing Re_λ, the range of shear in fully developed inertial-range turbulence expands in a cone. For $Re_\lambda < 50$ there is no inertial-range. The intersection of the two domains is the theoretically-realizable set of all planar IV turbulence measurements. The full range of S_T is measurable up to $Re_\lambda \cong 200$. The strongest vortices can still be accurately measured for $Re_\lambda \cong 5000$

Measurements corresponding to $\mathrm{Re}_\lambda \approx 100$ have been made for turbulent channel flow (Liu et al. 1991), where high resolution $4'' \times 5''$ sheet film allowed simultaneous capture of over 2 orders in scales with a single camera. If present, strong anisotropy of the flow field can be exploited, allowing multiple cameras to simultaneously resolved large and small scales, avoiding the extra cost of high resolution imaging sensors, as in the stratified flow experiments of Fincham et al. (1996) and Spedding et al. (1996a, b). By coupling a multiple camera system with some variable light sheet thickness optics, it would be possible to extend measurements into the $\mathrm{Re}_\lambda \approx 10^3$ range, using the approach discussed at the end of Sect. 4.2.1 along with currently existing algorithms.

5 Summary and conclusions

The CIV technique differs significantly from standard DPIV methods in several ways that together are responsible for order of magnitude improvements in accuracy and/or resolution on a given discretized image. Nevertheless, as does DPIV, CIV relies on image correlations, and most of the conclusions from the forgoing error analysis have quite broad applications amongst IV methods.

Fundamental limitations on the capability of current IV methods to accurately measure turbulent flows have been identified. Future progress depends entirely on continued improvements in the resolution of very small displacements, by increasingly sophisticated algorithms. But what is the theoretical limit? How accurate can an interpolative peak-fitting scheme be? It can be expected to depend on the information content of the original image which is

$$I_i = 2m \times n \times 2^p$$

for p-bit digitization on an $m \times n$ pixel array, assuming fully independent pixels. Such an image is not compressible. On similar grounds, one can express the information content of the estimated velocity field on an $M \times N$ grid as

$$I_v = 2M \times N \times \frac{(u_{\max} - u_{\min})}{\Delta u'},$$

(where $\Delta u'$ represents the uncertainty in u)

for both velocity components. If the information transmission ratio $I_v/I_i = 1$, all of the image information has been converted to velocity field estimates. Inserting some characteristic values gives $I_v/I_i = 0.01$, suggesting considerable theoretical room for improvement. Because advances in technology leading to improved image sensor characteristics only reduce E_{rms}, and not E_{mb}, which is insensitive to changes in B, the most

cost-effective way to climb up the Re($) curve is to improve algorithm accuracy, whose most serious limitation is caused by peak-locking errors. Our current efforts are therefore focused here. Once this hurdle is cleared it is expected that significant improvement in I_v/I_i can be obtained.

References

Adrian RJ (1988) Statistical properties of particle image velocimetry measurement in turbulent flow. In: Laser Anemometry in Fluid Mechanics, Vol. III. (Eds. Adrian, R.J. et al.) 115–130, Lisbon: Instituto Superior Tecnico, Ladoan

Adrian RJ (1991) Particle-imaging techniques for experimental fluid mechanics. Annu Rev Fluid Mech 23: 261–304

Browand FK; Plocher DA (1985) Image processing for sediment transport. Proceedings, 21st IAHR Congress, Melbourne, Australia, August 85, p. 7

Burt PJ; Yen C; Xu X (1982) Local correlation measures for motion analysis, a comparative study. IEEE Computer Society Conference on Pattern Recognition and Image Processing, Las Vegas, Nev.

Cowen EA; Monismith SG (1996) A hybrid digital particle tracking velocimetry technique. Exp Fluids, Submitted

Fincham AM; Spedding GR; Blackwelder RF (1991) Current constraints of digital particle tracking techniques in fluid flows. Bull Am Phys Soc 36: 2692

Fincham AM (1994) The structure of decaying turbulence in a stably stratified fluid, using a novel DPIV technique. PhD thesis Department of Aerospace Engineering, University of Southern California

Fincham AM; Maxworthy T; Spedding GR (1996) Energy dissipation and vortex structure in freely-decaying, stratified grid turbulence. Dyn Atmos Oceans 23: 155–169

Fuh CS; Maragos P (1991) Motion displacement estimation using an affine model for image matching. Optical Engineering 30: 881–887

Gilge M (1990) Motion estimation by scene adaptive block matching (SABM) and illumination correction. In: Image Processing Algorithms and Techniques, Proc. SPIE 1244, 355–366

Grant I (1994) Selected papers on Particle Image Velocimetry. SPIE Milestone Series, Vol. MS 99 SPIE, Washington

Hinze JO (1975) Turbulence. McGraw-Hill, New York

Huang HT; Fiedler HE; Wang JJ (1993) Limitation and improvement of PIV. Exp Fluids 15: 168–174

Jain JR; Jain AK (1981) Displacement measurement and its application to interframe coding. IEEE Trans. COM-29: 1799–1808

Kolmogorov AN (1941) Dissipation of energy in the locally isotropic turbulence. reprinted 1991. Proc R Soc Lond A 434: 15–17

Liu ZC; Landreth CC; Adrian RJ; Hanratty TJ (1991) High resolution measurement of turbulent structure in a channel with particle image velocimetry. Exp Fluids 10: 301–321

Lourenco L; Krothapalli A (1995) On the accuracy of velocity and vorticity measurements with PIV. Exp Fluids 18: 421–428

Monin AS; Yaglom AM (1975) Statistical Fluid Mechanics: Mechanics of Turbulence. MIT Press, Cambridge, MA

Prasad AK; Adrian RJ; Landreth CC; Offutt PW (1992) Effect of resolution on the speed and accuracy of particle image velocimetry interrogation. Exp Fluids 13: 105–116

Spedding GR; Rignot EJM (1993) Performance analysis and application of grid interpolation techniques for fluid flows. Exp Fluids 15: 417–430

Spedding GR; Browand FK; Fincham AM (1996) Turbulence, similarity scaling and vortex geometry in the wake of a towed sphere in a stably-stratified fluid. J Fluid Mech 314: 53–103

Spedding GR; Browand FK; Fincham AM (1996) The long-time evolution of the wake of a sphere in a stable stratification. Dyn Atmos Oceans 23: 171–182

Tennekes H; Lumley JL (1972) A First Course in Turbulence. MIT press

Tokumaru PT; Dimotakis PE (1995) Image correlation velocimetry. Exp Fluids 19: 1–15

Utami T; Ueno T (1984) Visualization and picture processing of turbulent flow. Exp Fluids 2: 25–32

Utami T; Ueno T (1987) Experimental study on the coherent structure of turbulent open-channel flow using visualization and picture processing. J Fluid Mech 174: 399–440

Utami T; Blackwelder RF; Ueno T (1990) Flow visualization with image processing of three-dimensional features of coherent structures in an open channel flow. In: Near wall turbulence. (Ed. Kline, S.J.) 289–305, Hemisphere, NY

Utami T; Blackwelder RF (1991) A cross-correlation technique for velocity field extraction from particulate visualization. Exp Fluids 10: 213–223

Westerweel J (1993) Analysis of PIV interrogation with low pixel resolution. Proc. SPIE-2005 Optical Diagnostics in Fluid and Thermal Flow, San Diego

Westerweel J (1994) Efficient detection of spurious vectors in particle image velocimetry data. Exp Fluids 16: 236–247

Willert CE; Gharib M (1991) Digital particle image velocimetry. Exp Fluids 10: 181–193